

Contents lists available at ScienceDirect

Wave Motion

journal homepage: www.elsevier.com/locate/wavemoti



Analytical extension of Finite Element solution for computing the nonlinear far field of ultrasonic waves scattered by a closed crack



P. Blanloeuil a,*, A. Meziane b, A.N. Norris c, C. Bacon b

- ^a School of Mechanical & Mining Engineering, University of Queensland, Brisbane, QLD 4072, Australia
- ^b University of Bordeaux, CNRS, Arts et Metiers ParisTech, I2M, UMR 5295, F-33400 Talence, France
- ^c Department of Mechanical and Aerospace Engineering, Rutgers University, Piscataway, NJ 08854-8058, USA

HIGHLIGHTS

- Computation of nonlinear scattering by closed cracks.
- Coupling of Finite Elements and analytical propagation.
- Crack modeled by unilateral contact with Coulomb's friction.
- Application to higher harmonics generation and non-collinear mixing of shear waves.

ARTICLE INFO

Article history: Received 24 December 2015 Accepted 14 April 2016 Available online 6 June 2016

Keywords:
Nonlinear acoustics
Scattering
Contact acoustic nonlinearity
Closed crack
Finite Element
Analytical propagation

ABSTRACT

Nonlinear scattering of ultrasonic waves by closed cracks subject to contact acoustic non-linearity (CAN) is determined using a 2D Finite Element (FE) coupled with an analytical approach. The FE model, which includes unilateral contact with Coulomb friction to account for contact between crack faces, provides the near-field solution for the interaction between in-plane elastic waves and a crack of different orientations. The numerical solution is then analytically extended in the far-field based on a frequency domain near-to-far field transformation technique, yielding directivity patterns for all linear and nonlinear components of the scattered waves. The proposed method is demonstrated by application to two nonlinear acoustic problems in the case of tone-burst excitations: first, the scattering of higher harmonics resulting from the interaction with a closed crack of various orientations, and second, the scattering of the longitudinal wave resulting from the nonlinear interaction between two shear waves and a closed crack. The analysis of the directivity patterns enables us to identify the characteristics of the nonlinear scattering from a closed crack, which provides essential understanding in order to optimize and apply nonlinear acoustic NDT methods.

© 2016 Elsevier B.V. All rights reserved.

1. Introduction

The detection of damage at early stage of fracture is of primary importance in many technologies, such as nuclear power plants or aeronautics. In the case of micro-cracks or closed cracks, the linear ultrasonic methods are less efficient but it has

E-mail address: p.blanloeuil@uq.edu.au (P. Blanloeuil).

st Corresponding author.

been proven in the past decade that nonlinear ultrasonics can bring an answer to this challenge. Many of these methods are based on the enrichment of the frequency content of the probing waves when interacting with the damage. The nonlinear effect involved in this interaction is related to contact dynamics and is called Contact Acoustic Nonlinearity (CAN) [1]. Sub- and higher-harmonic generation [1], frequency-modulation [2] have been shown to be sensitive to micro-cracks or closed cracks. For an overview of nonlinear acoustics applications see [3–5].

Numerically, both longitudinal and shear wave propagation through a rough surface were investigated in [6] using an interface contact model based on Hertz theory, for time harmonic incidence. The partial contact model was subsequently applied to model scattering from surface breaking cracks [7], and numerical simulations indicated efficient production of second harmonics. Another approach consists in introducing interface stiffness to account for quantitative transmission and reflection wave and harmonic generation [6,8,9]. Preisach-Mayergoyz space representation has been used to model CAN including hysteresis effect [10,11], and has also been implemented in time domain Finite Element (FE) model [12]. CAN has also been modeled by unilateral contact law with Coulomb's friction in time explicit Boundary Element Method (BEM) [13–15] or FE model [16]. In [13], the BEM was used for the study of SH slip motion on an arbitrary interface, which has later been extended to study of the interaction between a P wave or a SV wave with a pre-open or pre-stressed crack under normal incidence [14.15]. P waves correspond to longitudinal waves, whereas SH and SV waves correspond respectively to out-of-plane shear waves and in-plane shear waves. It was shown in [14,15] that the amplitudes of the higher harmonics of the scattered far-fields can be useful in determining both the pre-stress and the frictional coefficient. The same model was also used to treat the interaction between a crack and a SV wave for a given angle of incidence [15]. In this case, the crack was initially closed, and free of any pre-stress. The solution for the far field was obtained but the frequency content was not analyzed. It appears that considerable efforts have been made in previous work in order to model CAN but that the nonlinear far-field components have been only partially computed and that the nonlinear scattering patterns were not determined.

The purpose of this paper is to propose a generic method to compute the far field solution for the waves scattered by a closed crack when CAN is activated, including converted modes. In particular, the method is developed to provide a solution for the new frequency components generated by the contact dynamics triggered at the crack by the incident wave. Actually, for the development and the application of non-destructive methods based on nonlinear acoustics, it is fundamental to capture these new frequency components. Thus, the study scattering patterns corresponding to scattered higher harmonics is a valuable knowledge. Because no analytical solution is available for the contact dynamics problems, the first step of the method consists in using a 2D FE model to compute the near field solution in the time domain. The crack can be closed by a pre-stress and is modeled by a unilateral contact law with Coulomb friction. Once the solution for the scattered waves in the near field is obtained numerically, it is converted to the frequency domain and then extended in the far field domain using an analytical method. This second step uses Hankel's functions to compute the far field solution, which allows us to plot the directivity patterns of the scattered wave for different frequencies. This two step approach is similar to the one used by Hunt et al. to compute the linear field radiated from elastic structures in a fluid domain [17,18].

The paper is organized as follows. The two step method is described in Section 2, with first a description of the FE model, and second the analytical model used to propagate the solution in the far field. In Section 3, the method is applied to compute the directivity patterns for two examples of nonlinear acoustic problems. The first case is the nonlinear scattering of a wave by a closed crack of different orientations. The directivity patterns of the higher harmonics are obtained. The second case deals with the scattering of a longitudinal wave resulting from the interaction between two incident shear waves and a closed crack. This last example corresponds to an application of the non-collinear mixing method [19–22].

2. Computation of the nonlinear far field scattered waves

A two step procedure is proposed for computing the scattered far field resulting from the nonlinear interaction between one or two waves and a source of nonlinearity such as a closed crack. In this particular case, the contact dynamics generates the nonlinearity and therefore is the source of the higher harmonics. The proposed methodology allows us to plot the directivity patterns corresponding to the new generated frequency components. Longitudinal and shear waves can be scattered by the crack and the two modes are considered here.

The first step consists in using a FE model to treat the nonlinear interaction between an incident acoustic wave and a closed crack of finite extent, taking into account the contact dynamics. The FE model is solved using the code Plast2 [23]. The size of the FE model being limited in space due to computational cost, the numerical solution regarding scattered waves is restricted to the near field (a few wavelength away from the crack). To obtain the directivity pattern of the scattered waves and to gain understanding of the nonlinear scattering, the solution must be computed in the far field. The second step consists in extending the numerical solution in the far field based on analytical expressions. This is done for both longitudinal and shear scattered waves.

2.1. Finite element model for the near field solution

2.1.1. Problem statement and generic FE model

This section aims to describe the FE models used to treat the interaction between waves and a closed crack, including nonlinear effects due to the CAN. The description of the model is generic, giving the modeling principles, with some specific

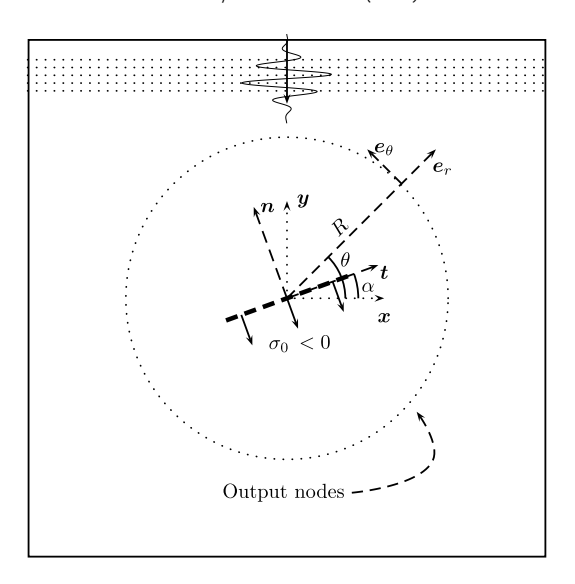


Fig. 1. Modeling of a wave interacting with a crack orientated by the angle α . The length of the crack is d = 10 mm. The crack is represented by the thick dashed line and a pre-stress σ_0 is applied on the interface. The numerical output is defined on a circle of radius R = 25 mm.

information such as geometrical dimensions or mesh size omitted here. These information will be given case by case in Section 3 where different examples are considered.

An isotropic and homogeneous solid is considered, its mechanical properties are those of aluminum. The Young's modulus is E=69 GPa, the Poisson's coefficient is $\nu=0.33$ and the density is $\rho=2700$ kg m $^{-3}$. This solid contains a crack that may be tilted by an angle α , and whose center defines the origin of the coordinate systems. The corresponding configuration is shown in Fig. 1 for a generic case. An acoustical wave is generated in the solid by imposing displacement on the top face. This wave is a sinusoidal tone burst windowed by a Hanning window. The wave propagates and interacts with the crack. The displacements are recorded at each node on a circle of radius R, as shown in Fig. 1. The contact dynamics triggered at the crack during the wave propagation is modeled by contact laws. They are described in the next section.

Spatial discretization is essential in the FE method. In order to have an accurate solution for the new higher frequency components generated by the CAN, the corresponding wavelengths have to be sufficiently discretized. If i is the number of the highest harmonic considered, then the corresponding wavelength λ_i has to be divided by at least 10 elements: $\lambda_i/a_{\text{max}} \geq 10$ where a_{max} is the maximal element dimension. That means that the FE mesh has to be defined depending on the highest frequency of interest. Convergence studies have been carried out in time and space to ensure that convergence was achieved. For all the considered models, the mesh is refined at the vicinity of the crack tips because of stress singularities ($\sigma \sim 1/\sqrt{r}$ where r is the radial distance from the crack tip). Again, the mesh refinement ensures the convergence as regards the wave propagation. Having an accurate estimation of the stress concentration at the crack tip is essential in fracture mechanics but out of the scope of this study. The mesh is made only of fully integrated quadrangle elements of type Q_1 [24]. The software Plast2 uses a time explicit integration scheme and therefore the time step is subject to the Courant–Friedrichs–Lewy stability condition $\Delta t \leq a_{\min} \sqrt{\rho/E}$, where a_{\min} corresponds to the smallest element dimension.

Finally, the scattered field is defined as the difference between the total field and the incident field (obtained without the crack). Therefore, two simulations have to be run to compute the scattered wave: with and without the crack. The displacements recorded at the selected output nodes for each simulation are subtracted to obtain the near field scattered waves in the time domain:

$$\mathbf{u}(R,\theta,t) = \mathbf{u}_T(R,\theta,t) - \mathbf{u}_I(R,\theta,t),\tag{1}$$

where $\mathbf{u}_T(R,\theta,t)$ is the total field and $\mathbf{u}_I(R,\theta,t)$ is the incident field. At this stage, the scattered displacement field contains information of both the scattered longitudinal and shear waves. The next section describes the contact laws used to model the contact dynamics on the crack.

2.1.2. CAN and contact laws

The contact dynamics generated along the crack is modeled by an interface of unilateral contact with Coulomb friction, which gives the relations between contact stresses and displacements at the interface. Three states can be observed simultaneously at different nodes of the interface: separation, slipping contact and sticking contact. The dynamic switching between the different contact states introduce the nonlinearity in the model. These boundary conditions can be referred as the non-smooth contact dynamics [25]. The crack can be either closed by the weight of the structure or an external load or a residual stress due to plasticity. Therefore, it is assumed that a static normal stress $\sigma_0 \le 0$ closes the crack. This pre-stress σ_0 is directly considered in the contact laws, as introduced in [16], and reviewed here briefly.

The two faces of the crack are denoted by i = 1, 2 respectively for the top and bottom face. Let be u^i the displacement and n^i the outward normal vector of the face i of the crack, the normal jump of displacements is defined by:

$$[u_n] = \mathbf{u}^1 \cdot \mathbf{n}^1 + \mathbf{u}^2 \cdot \mathbf{n}^2 = (\mathbf{u}^1 - \mathbf{u}^2) \cdot \mathbf{n}^1. \tag{2}$$

The incident wave creates stresses represented by the Cauchy stress tensor $\sigma(\mathbf{u}^i)$. Denoting $\sigma_n(\mathbf{u}^i)$ its normal component and $\tau(\mathbf{u}^i)$ its tangential component, the unilateral contact law taking into account σ_0 is given by the following equation:

$$\begin{cases}
\sigma_n(\mathbf{u}^i) + \sigma_0 \le 0 \\
[u_n] \le 0 \\
(\sigma_n(\mathbf{u}^i) + \sigma_0) \cdot [u_n] = 0.
\end{cases}$$
(3)

The first equation states that only a compression can be transmitted through the interface. The normal stress σ_n is allowed to be positive although the crack is closed as long as $\sigma_n \leq |\sigma_0|$. When $\sigma_n = -\sigma_0$ the interface opens. The second line corresponds to the non-penetration condition. Finally, the third line, or complementary equation, indicates that the contact interface is either open or closed.

Denoting μ the friction coefficient and $[u_t]$ the tangential jump of displacements, Coulomb's law is used for the tangential behavior. The pre-stress σ_0 is also introduced in the classical law:

$$\begin{cases} |\tau(\mathbf{u}^{i})| \leq \mu |\sigma_{n}(\mathbf{u}^{i}) + \sigma_{0}| \\ \text{If } |\tau(\mathbf{u}^{i})| < \mu |\sigma_{n}(\mathbf{u}^{i}) + \sigma_{0}| \Rightarrow \text{ sticking: } [u_{t}] = 0 \\ \text{If } |\tau(\mathbf{u}^{i})| = \mu |\sigma_{n}(\mathbf{u}^{i}) + \sigma_{0}| \Rightarrow \begin{cases} \text{sliding: } \exists \alpha \geq 0; [u_{t}] = -\alpha \tau(\mathbf{u}^{i}) \\ \tau(\mathbf{u}^{i}) = \pm \mu |\sigma_{n}(\mathbf{u}^{i}) + \sigma_{0}|. \end{cases}$$

$$(4)$$

The shear stress τ has to be equal to $\mu \mid \sigma_n + \sigma_0 \mid$ to generate sliding. When sliding occurs, the value of the shear stress now depends on the global normal stress $\sigma_n + \sigma_0$.

In Plast2, the contact algorithms are based on the forward Lagrange multipliers method [26] which enables the use of Lagrange multipliers in a time explicit integration. More precisely, the contact equations are respectively satisfied at time t and $t + \Delta t$. To make this possible, the contact equations are solved using a Gauss–Seidel iterative solver. The global method is thus semi-implicit. This method has been demonstrated to be robust [27]. The advantage of using Lagrange multipliers is that the above contact laws are strictly verified at each time step, which is essential for the modeling of the contact dynamics generated by the incident wave propagation.

2.2. Analytical solution for the radiated far field

The second step in computing the scattered far field resulting from the interaction between the incident wave and the crack consists of extending the numerical solution for the scattered waves in the outer domain using an analytical approach. Longitudinal and shear waves can be simultaneously scattered by the crack by virtue of mode conversion; the two modes have to be clearly distinguished. They propagate at different velocities and along different directions, as demonstrated later in Section 3. Therefore it is possible to select either one of the scattered wave modes by applying a time window based on the time of flight between the crack and the output nodes. A Hanning window spanning over N cycles is used for the pulse selection, where N=5 is the number of cycles of the incident wave if not stated otherwise. After time gating, the scattered displacement field is denoted \mathbf{u}^{β} , with $\beta=L$, S standing respectively for the longitudinal and the shear wave. Once the scattered mode is selected, radial and tangential displacements u_r^{β} and u_{θ}^{β} are computed using projection of displacements u_x^{β} . The mode separation will be demonstrated in Section 3.1.1.

The knowledge of the scattered field on the circle of radius R=25 mm is used to obtain the solution in the far field, assuming that the material has a linear behavior. The crack is considered like a secondary source located at the origin of the coordinate system. The considered scattered field $\mathbf{u}^{\beta}(R,\theta,t)$ obtained numerically in the time domain is converted into the frequency domain using the Fourier transform. Then, it is possible to derive the radiated field solution for $r \geq R$ from an integral equation at r=R. This kind of approach has already been used in fluid mechanics [17,18].

The solution is assumed to be time harmonic, with the time convention $e^{-i\omega t}$. In the frequency domain, the displacements are written as follows in polar coordinates:

$$\hat{\boldsymbol{u}}^{\beta}(r,\theta,\omega) = \hat{u}_{r}^{\beta}\boldsymbol{e}_{r} + \hat{u}_{a}^{\beta}\boldsymbol{e}_{\theta} = \nabla\phi + \nabla\wedge\psi\boldsymbol{e}_{z}, \quad r \geq R,$$
(5)

where ϕ and ψ are the velocity potentials respectively for the longitudinal wave and the shear wave. In the following, the mode identification β and the frequency dependence ω are omitted to lighten the notations. Then,

$$\hat{\boldsymbol{u}}(r,\theta) = \left(\frac{\partial \phi}{\partial r} + \frac{1}{r} \frac{\partial \psi}{\partial \theta}\right) \boldsymbol{e}_r + \left(\frac{1}{r} \frac{\partial \phi}{\partial \theta} - \frac{\partial \psi}{\partial r}\right) \boldsymbol{e}_\theta. \tag{6}$$

The velocity potentials have to satisfy the Helmholtz equation. Since we consider the waves scattered by a source located at the origin of the coordinate system, the potentials can be expressed as sum of Hankel's functions:

$$\begin{cases}
\phi = \sum_{n} \frac{A_{n}}{k_{L}} H_{n}^{(1)}(k_{L}r) e^{in\theta} + \frac{C_{n}}{k_{L}} H_{n}^{(2)}(k_{L}r) e^{in\theta} \\
\psi = \sum_{n} \frac{B_{n}}{k_{T}} H_{n}^{(1)}(k_{T}r) e^{in\theta} + \frac{D_{n}}{k_{T}} H_{n}^{(2)}(k_{T}r) e^{in\theta}
\end{cases} (7)$$

where the notation $\sum_n = \sum_{n=-\infty}^{+\infty}$ is used. The terms $k_L = \omega/c_L$ and $k_T = \omega/c_T$ are respectively the wave numbers for the longitudinal wave and the shear wave. The scattered waves have to satisfy the Sommerfeld condition, which states that the radiated energy should be outgoing at infinity. With the time dependence $e^{-i\omega t}$ and for a two dimensional space, this condition is given by:

$$\lim_{r \to \infty} \sqrt{r} \left(\frac{\partial}{\partial r} - ik \right) \hat{\boldsymbol{u}}(r, \theta) = 0.$$
 (8)

The Sommerfeld condition is obtained when $C_n = 0$, $D_n = 0$, $\forall n$. Replacing the potential expressions in Eq. (6), the radial and the tangential displacements are given by:

$$\begin{cases} \hat{u}_{r}(r,\theta) = \sum_{n} A_{n} H_{n}^{(1)'}(k_{L}r) e^{in\theta} + \frac{1}{r} \sum_{n} \frac{in}{k_{T}} B_{n} H_{n}^{(1)}(k_{T}r) e^{in\theta} \\ \hat{u}_{\theta}(r,\theta) = \frac{1}{r} \sum_{n} \frac{in}{k_{L}} A_{n} H_{n}^{(1)}(k_{L}r) e^{in\theta} - \sum_{n} B_{n} H_{n}^{(1)'}(k_{T}r) e^{in\theta}. \end{cases}$$
(9)

The coefficients A_n and B_n have now to be computed from an integral at r=R where the displacements are known. To do that, each term of Eq. (9) is multiplied by $e^{-im\theta}$ and integrated over the circular domain. Using the orthogonality of the functions $e^{in\theta}$ for the scalar product $\langle f,g\rangle=\int_0^{2\pi}f(\theta)g(\theta)d\theta$, we obtain:

$$\begin{cases}
\int_{0}^{2\pi} \hat{u}_{r}(R,\theta) e^{-im\theta} d\theta = 2\pi \left(A_{m} H_{m}^{(1)'}(k_{L}R) + \frac{im}{k_{L}R} B_{m} H_{m}^{(1)}(k_{T}R) \right) \\
\int_{0}^{2\pi} \hat{u}_{\theta}(R,\theta) e^{-im\theta} d\theta = 2\pi \left(\frac{im}{k_{L}R} A_{m} H_{m}^{(1)}(k_{L}R) - B_{m} H_{m}^{(1)'}(k_{T}R) \right),
\end{cases} \forall m.$$
(10)

Defining the matrix

$$\mathbf{M}_{n}(r) = \begin{pmatrix} H_{n}^{(1)'}(k_{L}r) & \frac{in}{k_{T}r}H_{n}^{(1)}(k_{T}r) \\ \frac{in}{k_{L}r}H_{n}^{(1)}(k_{L}r) & -H_{n}^{(1)'}(k_{T}r) \end{pmatrix}, \tag{11}$$

the coefficients A_n and B_n are the solution of a linear system, and are given by:

$$\begin{pmatrix} A_n \\ B_n \end{pmatrix} = \mathbf{M}_n^{-1}(R) \begin{pmatrix} \frac{1}{2\pi} \int_0^{2\pi} \hat{u}_r(R,\theta) e^{-in\theta} d\theta \\ \frac{1}{2\pi} \int_0^{2\pi} \hat{u}_\theta(R,\theta) e^{-in\theta} d\theta \end{pmatrix}.$$
(12)

Finally, the displacement field is obtained for any point of the outside domain from Eqs. (9) and (12):

$$\hat{\boldsymbol{u}}(r,\theta) = \sum_{n} \boldsymbol{M}_{n}(r) \boldsymbol{M}_{n}^{-1}(R) \frac{e^{\mathrm{i}n\theta}}{2\pi} \int_{0}^{2\pi} \hat{\boldsymbol{u}}(R,\theta') e^{-\mathrm{i}n\theta'} d\theta', \quad r \ge R, \forall \theta.$$
(13)

This solution is valid for a given frequency, which can be chosen as the fundamental frequency or one of the higher harmonics. Moreover, this solution corresponds either to the longitudinal or the shear wave depending on which mode has been selected initially from the numerical scattered field. The directivity patterns are obtained by plotting the amplitude of the displacements over $\theta \in [0; 2\pi]$ for any radial distance $r \geq R$. In the following, r denotes the distance used for the analytical computation whereas R is the radial distance where numerical output has been recorded.

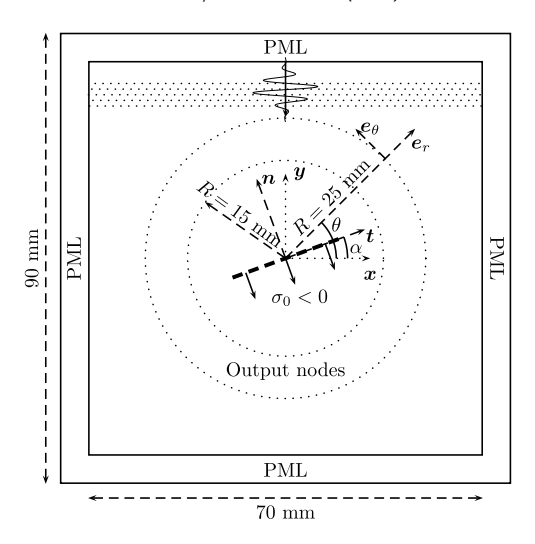


Fig. 2. Modeling of a wave interacting with a horizontal crack. The length of the crack is d = 10 mm. The numerical output is defined on two circles of radius R = 15 mm and R = 25 mm.

3. Directivity patterns for nonlinear scattering

3.1. Nonlinear scattering by a closed crack of various orientations

In this section, the interaction between a plane wave and a closed crack of different orientations is considered. The higher harmonics generated in the nonlinear scattering can be used for detection purposes. Directivity patterns corresponding to the higher harmonic components of the scattered waves are computed to provide some insight regarding their generation in the solid.

The modeling principles introduced in Section 2 are used here. The particular configuration of this example is shown in Fig. 2. The square aluminum solid contains a crack of 10 mm length tilted by an angle α . A Perfectly Matched Layer (PML) of 10 mm thickness is set around the solid to model an infinite medium. A 5-cycle tone burst plane wave windowed by a Hanning window is generated on the top face of the solid with an amplitude of 10 nm. The central frequency of this pulse is either 0.5 MHz or 1 MHz respectively for the generation of a shear wave or a longitudinal wave. The wavelength of the incident waves is thus $\lambda \simeq 6$ mm.

The maximal size of the elements is $a_{\rm max}=0.2$ mm which means that the wavelength of the third harmonic is divided into ten elements ($\lambda_3/a_{\rm max}\simeq 10$). The minimal size of the elements at the vicinity of the crack tips is $a_{\rm min}=0.07$ mm. The time step is $\Delta t=3$ ns, which satisfies the stability condition. Convergence in both time and space has been confirmed numerically. Finally, the numerical output is recorded on two circles of radius R=15 mm and R=25 mm, two circles being used for validation purposes.

3.1.1. Separation of the scattered modes

As mentioned in Section 2.2, the scattered field contains potentially both longitudinal and shear waves. The analytical method enables separate propagation of the scattered mode in the outer domain, based on the knowledge of the near field displacements expressed in polar coordinates. As explained before, it supposes that the longitudinal and the shear scattered waves can be separated in the time domain. This assumption is demonstrated here.

Fig. 3(a) shows a snapshot of the total displacement field after the interaction of an incident longitudinal wave with a crack tilted by $\alpha=25^\circ$. Although the baseline field has not been removed, one can clearly notice the reflected longitudinal wave followed by the mode converted shear wave. The two scattered pulses propagate with different velocities and along different directions. The output nodes are marked by the dotted circle, and the output node marked by the thick red disk is selected to plot time history displacements. As shown in Fig. 3(a), this node undergoes displacements from the two scattered modes. The corresponding displacements are plotted in Fig. 3(b). More precisely, the Cartesian displacement components u_x and u_y as well as the corresponding polar displacement components u_r and u_θ are shown for this output node. As expected, the two waves generate both u_x and u_y displacements. However, it can be seen that the two pulses are clearly separated. By contrast, the radial component corresponds only to the longitudinal wave whereas the tangential component corresponds mainly to the shear wave. The tangential displacement associated with longitudinal wave is negligible, and is due to miss-matching of the longitudinal wave front with the curvature of the sensor array and potential Poisson's effect for a non-purely cylindrical bulk wave. These results demonstrate that it is possible to separate the scattered modes in our case, and that the radial component provides a good representation of the longitudinal wave whereas the tangential component corresponds mainly to the shear wave.

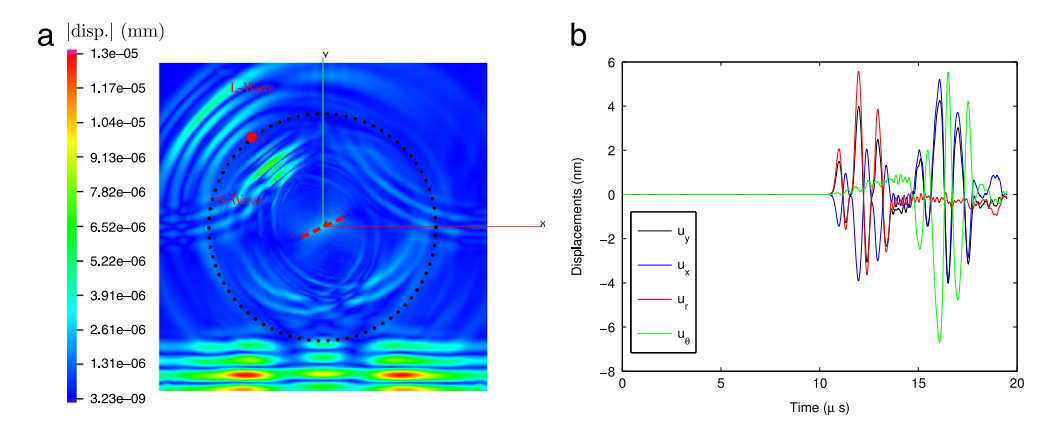


Fig. 3. (a) Total displacement field after interaction of the longitudinal wave with the crack, tilted by $\alpha=25^{\circ}$ at $t=13.6~\mu s$. The contact parameters are $\sigma_0=-0.15$ MPa and $\mu=0.8$. (b) Time history signals extracted from the red node shown in (a). (For interpretation of the references to color in this figure legend, the reader is referred to the web version of this article.)

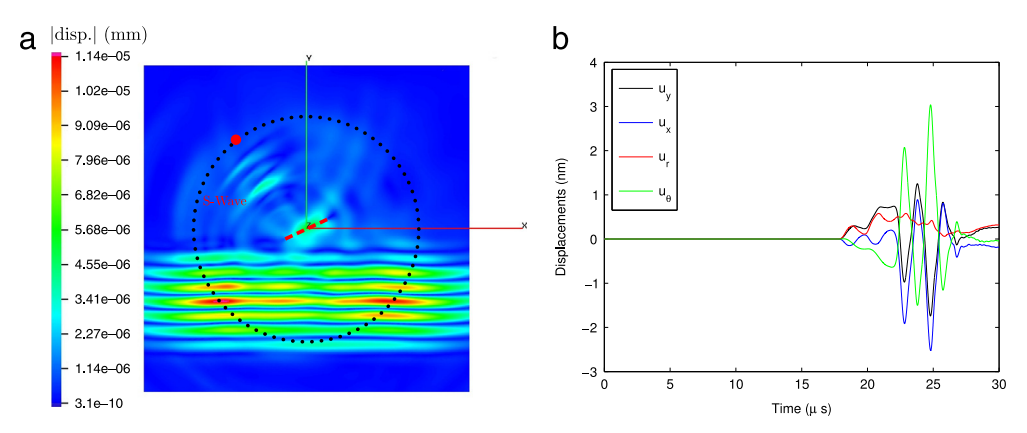


Fig. 4. (a) Total displacement field after interaction of the shear wave with the crack, tilted by $\alpha=25^{\circ}$ at t=21.6 μ s. The contact parameters are $\sigma_0=-0.25$ MPa and $\mu=0.3$. (b) Time history signals extracted from the red node shown in (a). (For interpretation of the references to color in this figure legend, the reader is referred to the web version of this article.)

The same effects can be seen in the case of an incident shear wave. Again, the separation of the scattered modes can be achieved for the same reasons, with waves propagating along different directions and at different velocities. The displacement field is shown in Fig. 4(a) straight after the interaction with crack. The reflected shear wave is clearly identified and the converted longitudinal wave is negligible with the contact parameters considered here. Thus, the mode separation is not a concern for this configuration. The same output node is selected to plot the time history signals in Fig. 4(b). The scattered shear wave is mainly described by the tangential component.

This validates the assumption of the mode separation. Thus, the analytical method can be applied to propagate either one of scattered mode after proper time selection. In the next section, the analytical propagation is validated.

3.1.2. Validation of the analytical propagation

The analytical propagation is validated by comparison with the FE solution at a same given distance of propagation. The numerical solution is extracted at nodes belonging to circles of radius R=15 mm and R=25 mm. The solution obtained at R=15 mm is propagated analytically to a distance r=25 mm which is then compared to the numerical solution obtained at the same distance. The case of a horizontal crack is considered here.

Fig. 5 shows the directivity patterns of the radial displacement u_r^L of the scattered longitudinal wave, in the case of an incident longitudinal wave. The directivity patterns are plotted for the fundamental, second and third harmonics, directly from numerical output at R=15 mm and R=25 mm as well as the one obtained after analytical propagation at a distance of 25 mm. All directivity patterns are normalized by their respective maximal amplitude for the sake of clarity. The incident wave propagates along $-\boldsymbol{y}$ which corresponds to the direction 270° and the contact parameters are $\sigma_0=-0.15$ MPa and $\mu=0.8$.

The scattered field computed analytically at r = 25 mm from the numerical output obtained at R = 15 mm matches the numerical result extracted at R = 25 mm, which confirms the proposed method. Also, by comparing the data obtained for two propagation distances, it can be seen that the amplitude of the scattered wave decreases with the propagation distance as expected.

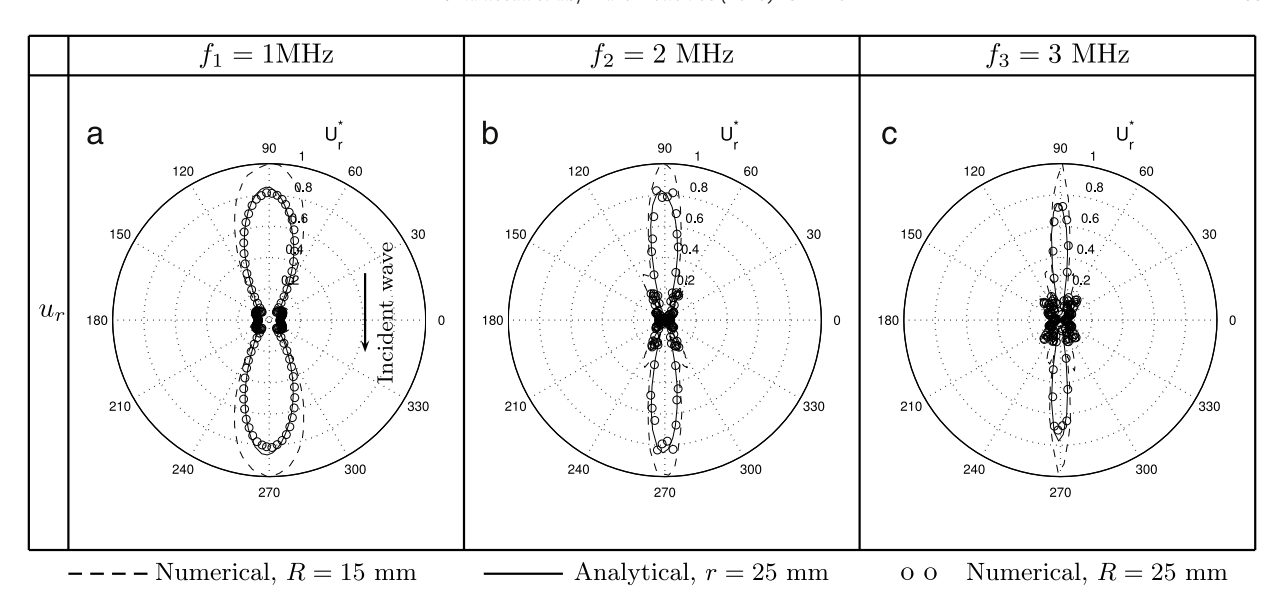


Fig. 5. Directivity patterns of the longitudinal wave scattered by a horizontal crack for the first three harmonics, obtained numerically at R=15 mm and R=25 mm as well as the one obtained analytically at r=25 mm from numerical data at R=15 mm. $\sigma_0=-0.15$ MPa and $\mu=0.8$.

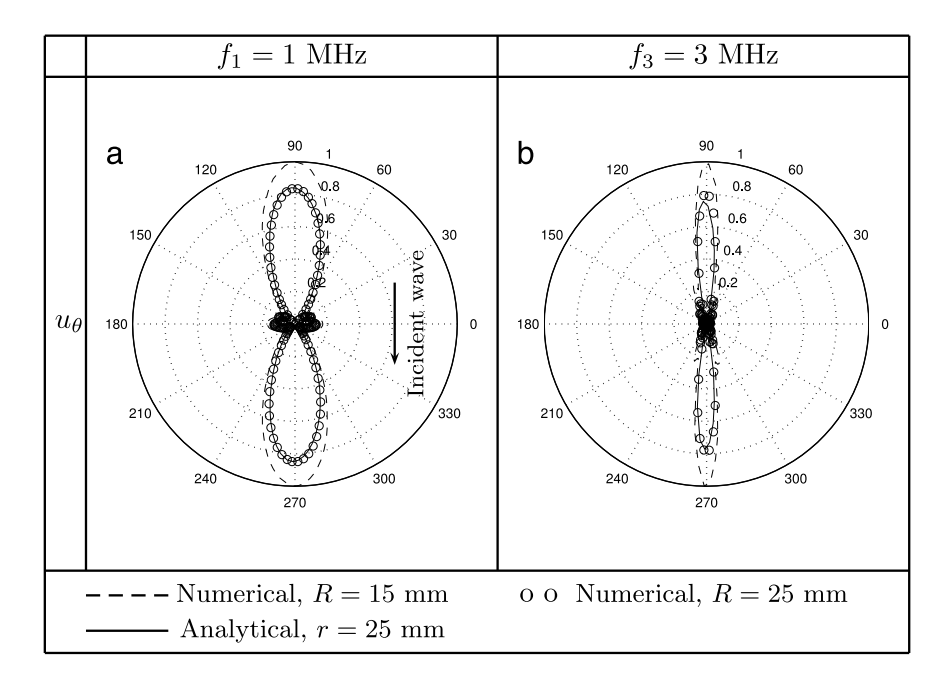


Fig. 6. Directivity patterns of the shear waves scattered by a horizontal crack for the first and the third harmonic, obtained numerically at R=15 mm and R=25 mm as well as the one obtained analytically at r=25 mm from numerical data at R=15 mm. $\sigma_0=-0.25$ MPa and $\mu=0.3$.

An incident shear wave is now considered, still with a horizontal crack, and with a pre-stress $\sigma_0 = -0.25$ MPa and a coefficient of friction $\mu = 0.3$. Fig. 6 shows the directivity patterns of the tangential displacement u_{θ}^{S} of the scattered shear wave, for the fundamental and the third harmonic only. The directivity pattern of the second harmonic is not relevant since the generation of second harmonic is negligible in the case of a shear wave interacting with a contact interface under normal incidence, as demonstrated in [28,29] and later on in Fig. 8(e). All directivity patterns are normalized by their respective maximal amplitude.

The analytically propagated solution matches the numerical results, for the first and the third harmonic. This validates the method for the analytical propagation of shear waves.

3.1.3. Various crack orientations and in-plane longitudinal wave

When the crack is not horizontal, it is expected that the interaction with the incident wave leads to mode conversions. The directivity patterns are used to identify the directions of propagation of those converted modes. In the following, only the main displacement component generated by each of these modes is considered: u_r^L and u_θ^S . They correspond respectively to radial displacements created by the longitudinal scattered wave and tangential displacements created by the scattered shear waves. The directivity patterns are normalized by the maximal displacement measured at r=R in the case of a linear simulation, *i.e.* with free boundary conditions applied to the crack faces. The numerical data obtained at R=25 mm is used for the analytical propagation at a distance of r=100 mm.

Fig. 7 shows the directivity patterns plotted in the far field for the fundamental frequency and the two first higher harmonics, for three orientations of the crack: $\alpha=0^\circ$, 25°, 45°. The contact parameters are $\sigma_0=-0.15$ MPa and $\mu=0.8$. The directions of propagation predicted by the classical Snell's law (reflection and transmission at a perfect infinite interface) are marked by the arrows. Mode conversion to shear wave occurs only for oblique incidence, since no tangential displacement is created at the contact interface for a normal incidence. Considering the fundamental frequency, the scattered waves propagate closely to directions given by the transmission–reflection laws, with deviation of a few degrees for the longitudinal component. The second and the third harmonics are generated by the CAN occurring at the crack interface. These harmonics propagate exactly along directions predicted by the transmission–reflection laws and no deviation is observed. The directivity is enhanced in the case of higher harmonics because of the shorter wavelength. If one wants to move on experimental application, it means that the placement of the transducers for nonlinear experiment should be checked precisely, as demonstrated in [30]. The amplitude of the harmonics contained in the shear waves increases with the angle of incidence whereas it decreases for the reflected longitudinal waves. The mode conversion is stronger for high angle of incidence and this is observed for the fundamental and the higher harmonics.

The differences in the agreement of the directions of propagation with those obtained by considering Snell's law are related to the product between the wavenumber k and the crack length d. It has been shown in [31] that the directions of propagation of the reflected and transmitted waves increasingly deviate from the Snell's law predictions as the value of kd decreases, with good agreement above $kd \simeq 20$ for incident longitudinal waves and $kd \simeq 40$ for incident shear waves. Considering the current parameters, the product kd is above 20 for the higher harmonics as well as for the shear wave at the fundamental frequency, whereas the value is around 10 for the longitudinal component at the fundamental harmonic. Thus, directions of propagation slightly deviate from the reflection—transmission law for the longitudinal scattered wave at the fundamental frequency.

3.1.4. Various crack orientations and incident in-plane shear wave

An incident shear wave is now considered. The directivity patterns computed analytically in the far field at r=100 mm from data recorded at R=25 mm are plotted in Fig. 8 for three crack orientations: $\alpha=0^{\circ}$, 25° , 45° . The directivity patterns are normalized by the maximal displacement measured at r=R in the case of a linear simulation, *i.e.* with free boundary conditions applied to the crack faces. The contact parameters are $\sigma_0=-0.25$ MPa and $\mu=0.3$. In this case, the incident normal stress is too low to activate the clapping and only sliding is activated at the interface whatever the angle of incidence [16]. The directions of propagation corresponding to the transmission through a perfect interface and the reflection at a free surface are marked by the arrows.

Similarly to the longitudinal wave, there is no mode conversion under normal incidence. For an oblique incidence $(\alpha=25^\circ)$ the mode conversion occurs but the amplitude of the longitudinal waves is weak compared to those of the shear waves. This result holds for the current contact parameters and a different pre-stress may change the amplitude of the converted mode. For the fundamental frequency, a deviation from the direction obtained with the transmission–reflection laws is again observed with a maximal difference of 10° for the forward scattered shear wave. As explained before, this is accounted for by relatively large wavelength compared with the crack length, where the value of kd is around 10 for this incident shear wave of 0.5 MHz. Those deviations die out as the frequency increases and the higher harmonics, when they are generated, follow the directions of propagation given by the Snell's law.

One can see that under normal incidence, the third harmonic is preferentially generated for the tangential displacements as already demonstrated in [28,29]. For $\alpha=25^\circ$, mode conversions occur and the second harmonic amplitude is now at the same order as the third harmonic. For $\alpha=45^\circ$ the values of all harmonics are negligible because there are actually no scattered waves. The reason can be understood under the consideration of contact stresses. The in-plane shear wave generates a shear stress $\sigma_{xy}(t)$ in the solid whose maximal amplitude is 0.23 MPa for the considered incident shear wave. The normal and tangential stress generated by the incident wave at the interface are given by:

$$\begin{cases} \sigma_n^{inc}(t) = (\boldsymbol{\sigma}(t).\boldsymbol{n}).\boldsymbol{n} = -\sigma_{xy}(t)\sin 2\alpha \\ \tau^{inc}(t) = (\boldsymbol{\sigma}(t).\boldsymbol{n}).\boldsymbol{t} = \sigma_{xy}(t)\cos 2\alpha \end{cases}$$
(14)

where σ is the stress tensor and \boldsymbol{n} and \boldsymbol{t} are respectively the normal and tangent vector at the interface. For $\alpha=45^\circ$, the shear stress $\tau^{inc}(t)$ becomes zero and consequently it cannot trigger sliding at the interface. The normal stress being too small to open the crack where a static compression of $\sigma_0=-0.25$ MPa is considered, there is no nonlinear effect and the wave propagation is not affected by the crack.

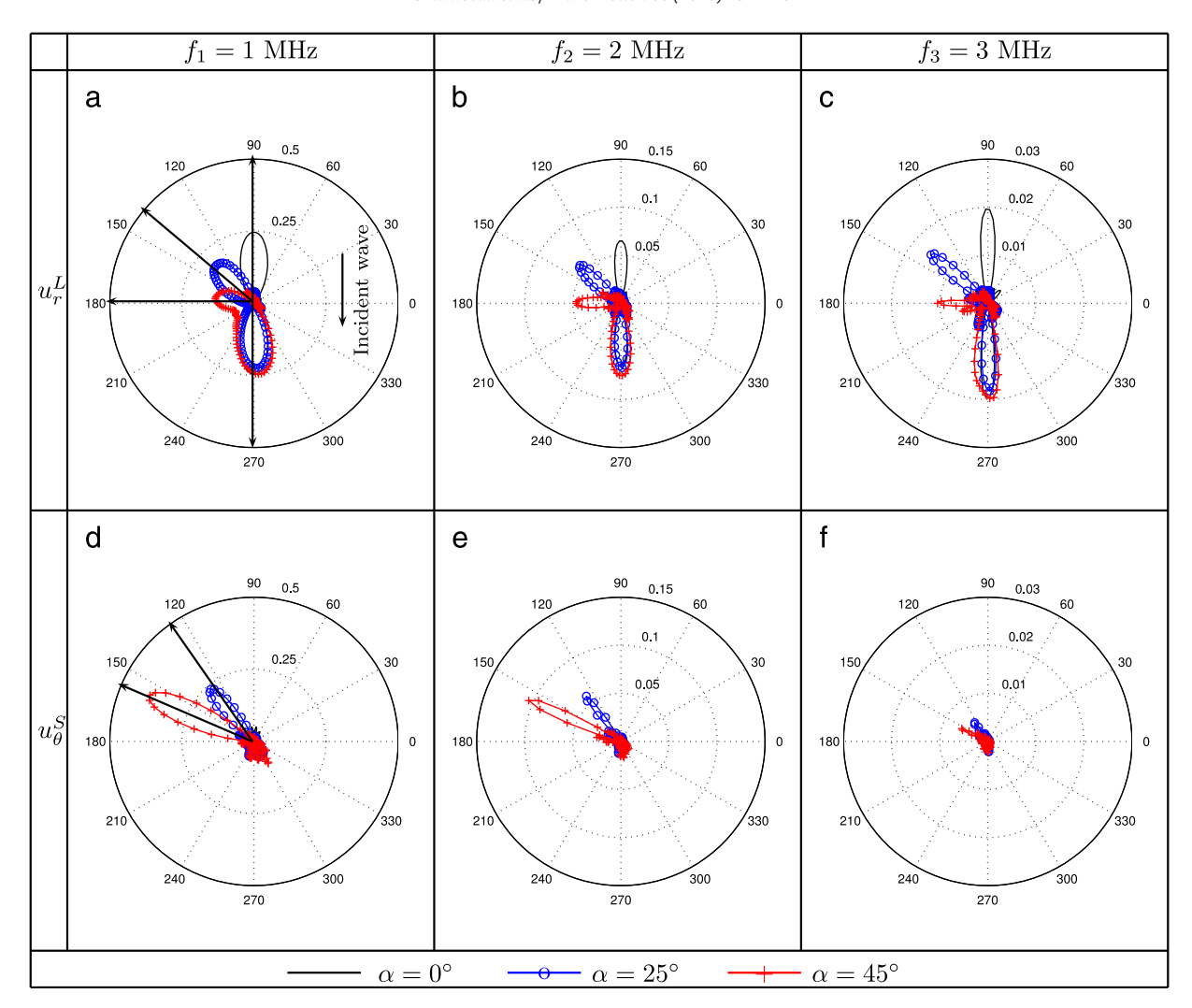


Fig. 7. Directivity patterns of the scattered longitudinal and shear waves for an incident longitudinal wave, for $\alpha=0^{\circ}$, 25° , 45° , (a), (b) and (c) give the radial displacements \boldsymbol{u}_{r}^{S} for the fundamental and the two first higher harmonics. (d), (e) and (f) give the tangential displacements $\boldsymbol{u}_{\theta}^{S}$ for the same frequencies. $\sigma_{0}=-0.15$ MPa and $\mu=0.8$.

This example shows how the proposed method enables the study of the higher harmonics generated by the CAN for a crack of arbitrary orientation. The new nonlinear frequency components of the scattered waves provide information that can be useful for closed crack detection purposes.

3.2. Nonlinear interaction of two shear waves under oblique incidence

In this section the interaction between two incident shear waves and a closed crack is investigated. Because of nonlinearity, the principle of superposition is no longer satisfied and acoustic waves can interact with each other [32]. If some conditions regarding the ratio of input frequencies, the angles of incidence and the wave polarization are found in combination, this interaction can lead to the generation of a third wave. This wave has a frequency and a wave-vector equal to the sum of the incident frequencies and wave-vectors respectively [32]. Also, the polarization of the generated wave is different from those of the incident waves. This arrangement is referred to as the non-collinear mixing technique.

The method offers some advantages over the more conventional nonlinear harmonic generation technique or nonlinear wave modulation techniques. It provides modal selectivity (the wave resulting of the nonlinear mixing is a different mode to the incident waves), frequency selectivity (the frequency of the scattered wave is equal to the sum of the input frequencies) and directional selectivity (the scattered signal propagates in a different direction from the incident waves). The phenomenon was first demonstrated experimentally by Rollins [33]. More recently, the scattered wave has been used to evaluate plastic deformation in an aluminum solid [19]. The method has also been successfully applied to the evaluation of physical aging of PVC [20], the evaluation of a diffusion welding interface in titanium [21], and more recently to imperfect interfaces [34] and closed cracks [22].

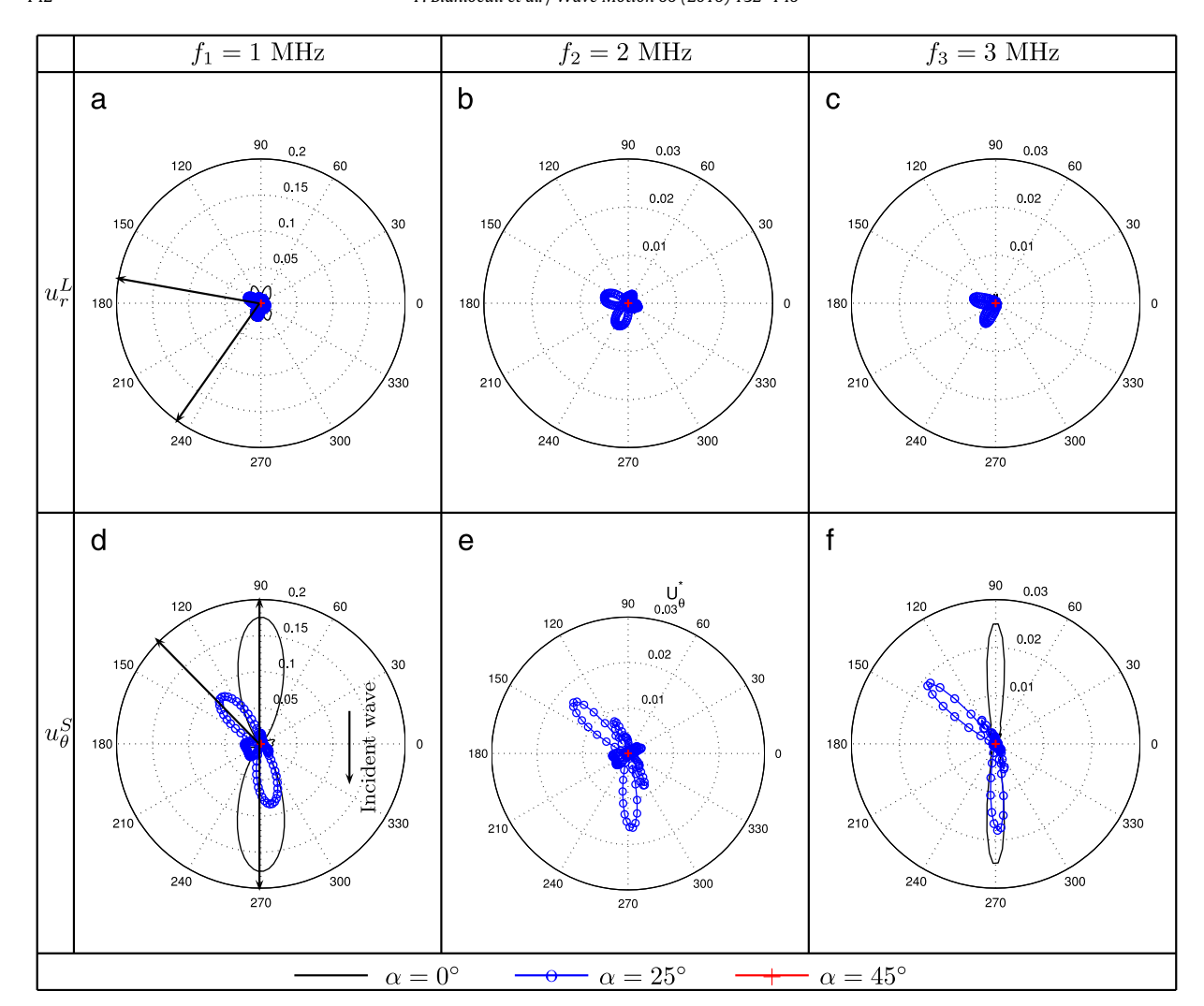


Fig. 8. Directivity patterns of the scattered longitudinal and shear waves for an incident shear wave, for $\alpha=0^\circ, 25^\circ, 45^\circ$. (a), (b) and (c) give the radial displacements $\boldsymbol{u}_r^{\varsigma}$ for the fundamental and the two first higher harmonics. (d), (e) and (f) give the tangential displacements $\boldsymbol{u}_{\theta}^{\varsigma}$ for the same frequencies. $\sigma_0=-0.25$ MPa and $\mu=0.3$.

The method described in Section 2 is used to predict the direction of propagation of the longitudinal scattered wave generated by the interaction of two incident shear waves with a closed crack. The configuration of the system is shown in Fig. 9. The crack is 20 mm long and is located at the center of the solid and two in-plane shear waves (A and B) are excited at the top face with an angle of incidence θ_l with respect to the $\bf y$ axis. Different time delays are applied to the top nodes to generate the incident waves with the chosen angle of incidence. The distance between the source and the angle of incidence is chosen so that the waves intersect at the crack. The distance between the source is set to 120 mm which gives an angle of incidence $\theta_l = 55^{\circ}$.

The incident shear waves are pulses of 5 cycles with a frequency of 1 MHz and amplitude of 10 nm. Note that the same input frequencies are chosen for the sake of simplicity regarding the following analysis, whereas in practical application the frequency selectivity would be enhanced by choosing different input frequencies. A pre-stress $\sigma_0 = -0.1$ MPa and friction coefficient $\mu = 0.5$ are considered at the crack interface. It is expected that this combination of waves leads to the generation of a longitudinal wave with the frequency of 2 MHz when clapping is activated [22]. To model accurately the wave propagation, the maximal element size of the FE model is set to 0.15 mm thus ensuring that the minimal wavelength considered in this study is discretized by at least 10 elements. Displacements recorded on the circle of radius R = 25 mm are used to compute the directivity patterns of the scattered waves in the far field at r = 100 mm, using the method presented previously. As previously done in Section 3.1.1, the separation of the scattered longitudinal and shear waves in the time domain has been verified to ensure the applicability of the method.

The directivity patterns for two incident shear waves and three crack orientations $\alpha=0^{\circ}$, 10° and 20° are plotted respectively in Figs. 10-12. Radial displacements u_r^L of the longitudinal scattered waves and tangential displacements u_s^Q

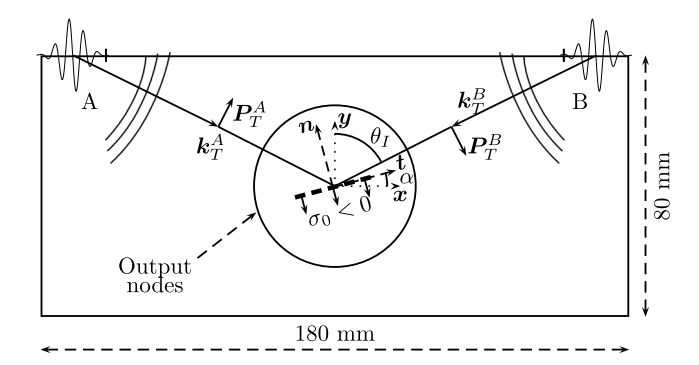


Fig. 9. Modeling of two shear waves interacting with a closed crack orientated by the angle α . The length of the crack is d=20 mm. The two shear waves are generated from the top face with an oblique incidence $\theta_l=55^\circ$ such that they intersect at the crack.

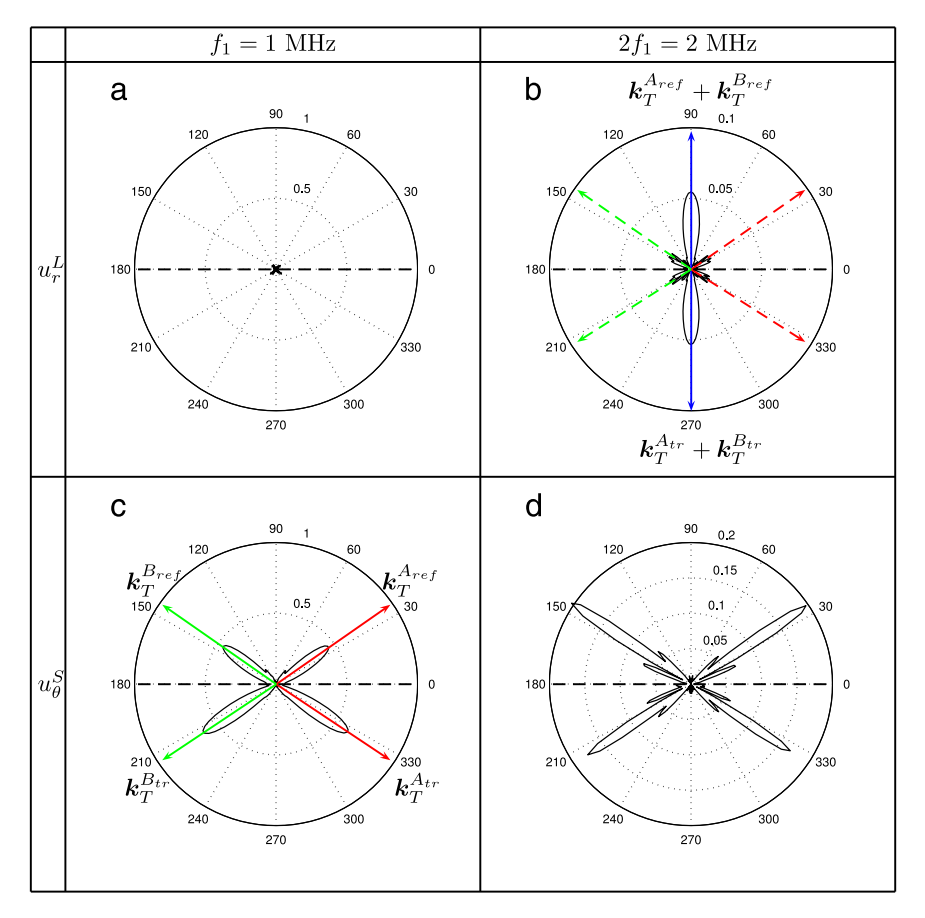


Fig. 10. Directivity patterns for two incident shear waves for $\alpha=0^\circ$. Radial displacements \boldsymbol{u}_T^L and tangential displacements \boldsymbol{u}_T^S are plotted for the fundamental frequency and twice the fundamental. Directions of propagation of the reflected $(\boldsymbol{k}_T^{Aref})$ and \boldsymbol{k}_T^{Bref} and \boldsymbol{k}_T^{Aref} and \boldsymbol{k}_T^{Bref}) shear waves predicted by Snell's law are represented by arrows (c). Longitudinal waves are scattered for $2f_1$ in two directions collinear to $\boldsymbol{k}_T^{Aref} + \boldsymbol{k}_T^{Bref}$ and $\boldsymbol{k}_T^{Aref} + \boldsymbol{k}_T^{Bref} + \boldsymbol{k}_T^{Bref}$ and $\boldsymbol{k}_T^{Aref} + \boldsymbol{k}_T^{Bref} + \boldsymbol{k}_T^{Bref} + \boldsymbol{k}_T^{Bref} + \boldsymbol{k}_T^{$

of the scattered shear waves are normalized by the maximal displacement obtained for the linear simulation, *i.e.* with free boundary conditions applied to the crack faces and for a crack orientation of $\alpha=0^{\circ}$. The main directions of propagation are marked by arrows. The directivity patterns are plotted for the fundamental frequency ($f_1=1$ MHz) and the double frequency ($f_1=1$ MHz).

The directivity patterns obtained for $\alpha=0^\circ$ are shown in Fig. 10. At the fundamental frequency f_1 , there is no longitudinal waves (Fig. 10(a)) and only reflected and transmitted shear waves are propagating (Fig. 10(c)). Directions of propagation of the reflected shear waves ($\mathbf{k}_T^{A_{ref}}$ and $\mathbf{k}_T^{B_{ref}}$) and transmitted shear waves ($\mathbf{k}_T^{A_{tr}}$ and $\mathbf{k}_T^{B_{tr}}$) conform with the reflection from a free surface and a transmission through a perfect interface. This agrees with the previous observation regarding the value of the

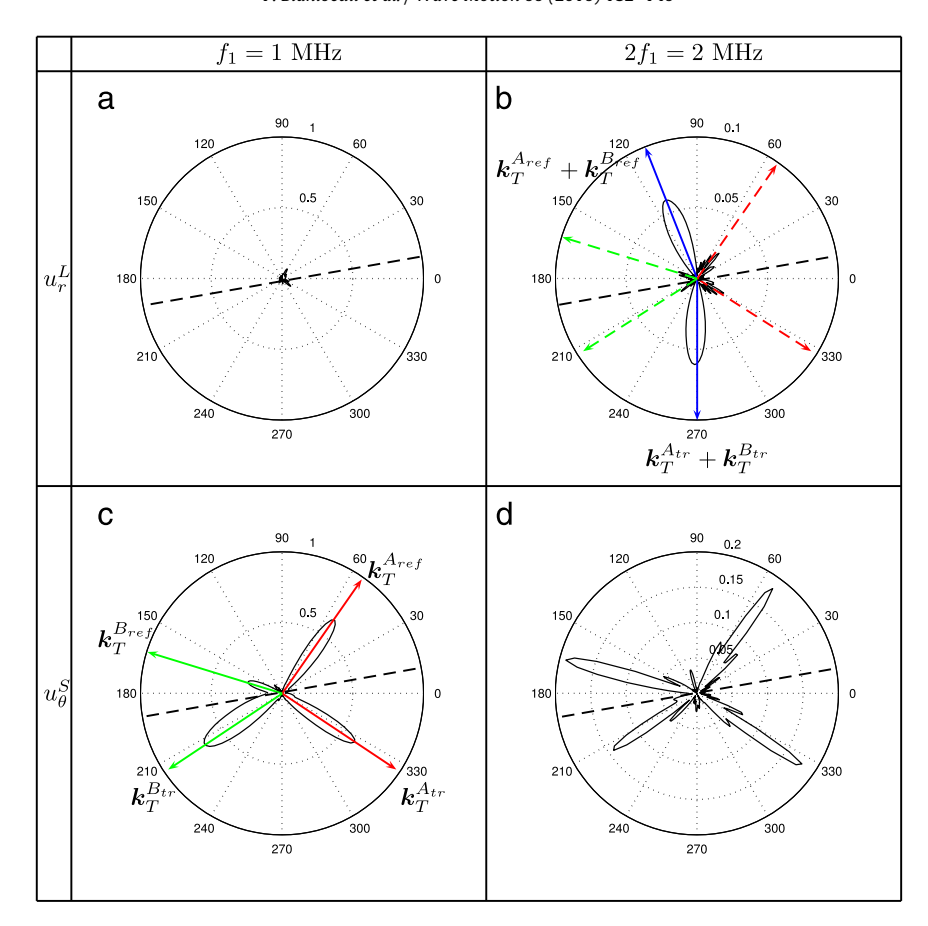


Fig. 11. Directivity patterns for two incident shear waves for $\alpha=10^\circ$. Radial displacements \boldsymbol{u}_r^L and tangential displacements \boldsymbol{u}_r^S are plotted for the fundamental frequency and twice the fundamental. Directions of propagation of the reflected $(\boldsymbol{k}_T^{A_{ref}}$ and $\boldsymbol{k}_T^{B_{ref}})$ and transmitted $(\boldsymbol{k}_T^{A_{tr}}$ and $\boldsymbol{k}_T^{B_{tr}})$ shear waves predicted by Snell's law are represented by arrows (c). Longitudinal waves are scattered for $2f_1$ in two directions collinear to $\boldsymbol{k}_T^{A_{trf}} + \boldsymbol{k}_T^{B_{trf}}$ and $\boldsymbol{k}_T^{A_{tr}} + \boldsymbol{k}_T^{B_{tr}}$ and $\boldsymbol{k}_T^{A_{tr}} + \boldsymbol{k}_T^{B_{tr}} + \boldsymbol{k}_T^{B_{tr}}$ and $\boldsymbol{k}_T^{A_{tr}} + \boldsymbol{k}_T^{B_{tr}} + \boldsymbol{k}_T^{B_$

kd value, with $kd \simeq 40$. There is no converted longitudinal wave at the fundamental frequency because the angle of incidence is greater than the critical angle. Due to the CAN at the crack, the second harmonic $(2f_1)$ is generated in both reflected and transmitted shear waves as shown in Fig. 10(d). Finally, at the double frequency $2f_1$, two longitudinal waves propagate respectively along directions 90° and 270° . These waves result from the nonlinear interaction between the incident shear waves and are the ones targeted in the non-collinear mixing method.

Because the crack partially opens during the acoustic excitation, the incident waves are partially reflected as shown in Fig. 10. Locally, the shear waves constructively interact at the contact interface when the clapping is activated, which generates two longitudinal waves. The first one propagates along a direction collinear with $\mathbf{k}_T^{A_{tr}} + \mathbf{k}_T^{B_{tr}}$. The second one propagates in a direction collinear with the sum of the reflected wave vectors $\mathbf{k}_T^{A_{ref}} + \mathbf{k}_T^{B_{ref}}$.

The directivity patterns obtained in the case of a crack tilted by an angle $\alpha = 10^\circ$ are given in Fig. 11. Because of the

The directivity patterns obtained in the case of a crack tilted by an angle $\alpha=10^\circ$ are given in Fig. 11. Because of the crack orientation, the angles of incidence with respect to the normal direction to the contact interface are different for the two incident waves. For the fundamental frequency, the transmitted shear waves have the same directions of propagation as the incident waves, as obtained previously for $\alpha=0^\circ$. The reflected waves still propagate along directions predicted by Snell's laws (Fig. 11(c)). There is still no longitudinal wave at this frequency (Fig. 11(a)). For the double frequency, two longitudinal waves are again generated (Fig. 11(b)) and propagate along directions given by the sum of the transmitted wave vectors $\mathbf{k}_T^{A_{rr}} + \mathbf{k}_T^{B_{tr}}$ and reflected wave vectors $\mathbf{k}_T^{A_{ref}} + \mathbf{k}_T^{B_{ref}}$ which is no longer collinear with the normal vector to the contact interface.

Fig. 12 shows the directivity patterns for the case of a crack tilted by an angle $\alpha=20^\circ$. For the fundamental frequency, a longitudinal wave is observed along 20° direction due to conversion of shear wave A (Fig. 12(a)). Snell's law indicates a critical incident angle of 30° (incident shear wave A has an incident angle of 35°, thus conversion is possible due to finite aperture of the incident wave beam). Shear waves A and B are reflected and transmitted with direction predicted by the reflection–transmission laws. However, because of the high angle of incidence, the directions of transmission and reflection of the incident shear wave B are close and not easily distinguished for the fundamental harmonic. This leads to a single lobe

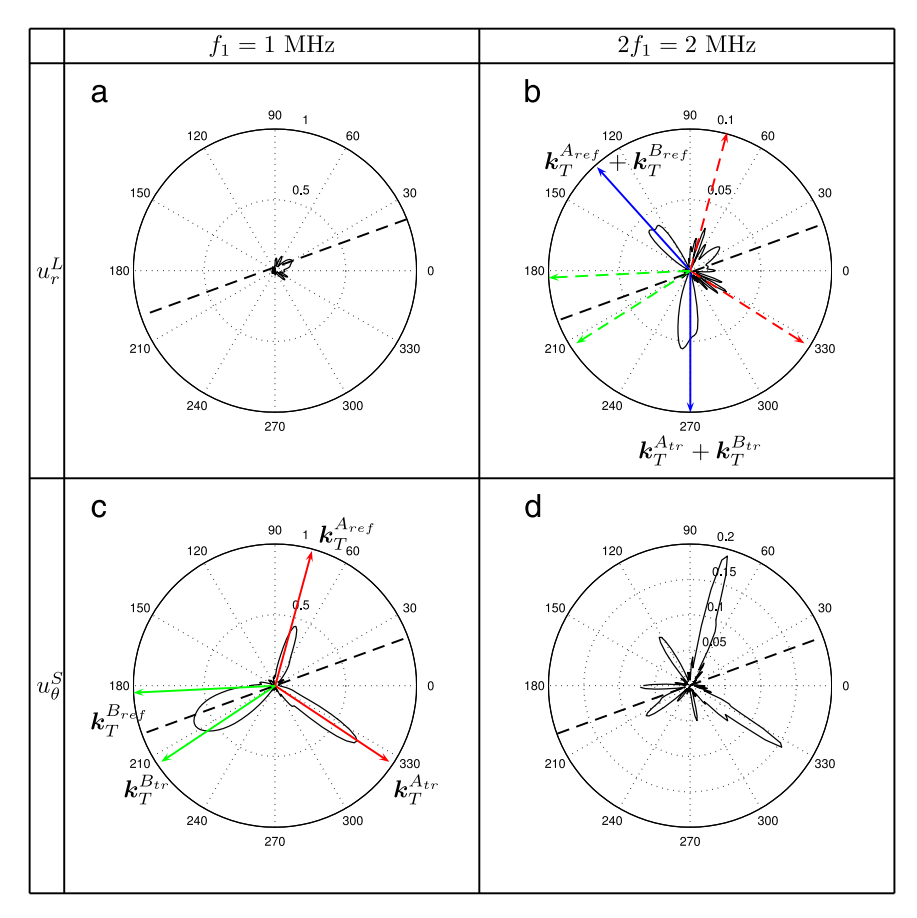


Fig. 12. Directivity patterns for two incident shear waves for $\alpha=20^{\circ}$. Radial displacements \boldsymbol{u}_{T}^{L} and tangential displacements \boldsymbol{u}_{S}^{0} are plotted for the fundamental frequency and twice the fundamental. Directions of propagation of the reflected $(\boldsymbol{k}_{T}^{Arg}$ and $\boldsymbol{k}_{T}^{Brg})$ and transmitted $(\boldsymbol{k}_{T}^{Arg}$ and $\boldsymbol{k}_{T}^{Brg})$ shear waves predicted by Snell's law are represented by arrows (c). Longitudinal waves are scattered for $2f_{1}$ in two directions collinear to $\boldsymbol{k}_{T}^{Arg}+\boldsymbol{k}_{T}^{Brg}$ and $\boldsymbol{k}_{T}^{Arg}+\boldsymbol{k}_{T}^{Brg}$ and $\boldsymbol{k}_{T}^{Arg}+\boldsymbol{k}_{T}^{Brg}$ and $\boldsymbol{k}_{T}^{Arg}+\boldsymbol{k}_{T}^{Brg}$ and $\boldsymbol{k}_{T}^{Arg}+\boldsymbol{k}_{T}^{Brg}$ and $\boldsymbol{k}_{T}^{Arg}+\boldsymbol{k}_{T}^{Brg}$

in the directivity pattern at an intermediate angle around 205°. By contrast, the two directions are clearly separated for the second harmonic, as shown in Fig. 12(d). For the double frequency, two longitudinal waves are again generated (Fig. 12(b)) and propagate along directions given by the sum of the transmitted wave vectors $\mathbf{k}_T^{Arr} + \mathbf{k}_T^{Br}$ and reflected wave vectors $\mathbf{k}_T^{Aref} + \mathbf{k}_T^{Br}$. In Fig. 12(d), it can be seen that two additional shear waves are propagating along 120° and 280° directions although their amplitude is relatively small. These shear waves correspond of the mode conversion from the longitudinal waves nonlinearly generated at the crack interface. The magnitude of these last shear waves also depends on the value of the pre-stress σ_0 at the interface.

These examples demonstrate that the use of the FE method coupled to analytical propagation provides understanding of the wave scattering for complex wave propagation problems involving CAN and multiple wave interactions. It very effectively shows the directions of propagation of scattered waves in the case of the non-collinear mixing method. The CAN is a non-classical nonlinearity and involves specific scattering of longitudinal and shear waves, especially in the case of tilted cracks. This method can be used with may help to define and optimize the non-collinear mixing method in the case of different input frequencies.

4. Conclusion

In this paper a method is proposed to derive the directivity patterns for waves scattered after nonlinear interaction with a closed crack, thus giving information about the expected wave fields both in the near and far-field of cracks with contact nonlinearity. The method includes two steps to compute the far field solution. Since the CAN generated from the interaction between the incident wave and the defect cannot be described analytically, the first step of the method consists in computing the near field solution with a FE model. The CAN is modeled using unilateral contact law with Coulomb friction. In the second step, the numerical solution for the scattered waves is propagated analytically in order to obtain the far field solution. This is achieved using a Green's function formalism in the frequency domain, thus giving the solution for any considered frequency

of interest. This makes the method particularly interesting for the study of nonlinear problems involving a closed crack where new frequency components are generated.

In the second part of this paper, the method was first applied to the nonlinear scattering of a plane wave by a closed crack of different orientations. The propagation direction of the higher harmonics has been obtained for the incident mode as well as the converted mode, both for an incident longitudinal and an incident shear wave. Then, the method was applied to predict the direction of propagation of the longitudinal wave scattered by the interaction of two incident shear waves, such as proposed for the non-collinear mixing method. The method can be used to determine when the longitudinal wave is generated in case of CAN, as well as its directions of propagation for complex configuration where the crack is tilted.

The application of the method can be extended to other problems. Knowledge of the scattering by a closed crack in case nonlinearity can be used to derive an imaging algorithm based on the higher harmonics. For the non-collinear mixing, the method enables one to predict the solution in the case of different incident waves (frequency and angle of incidence). The method could also be used to work with the side-band frequency components generated during the nonlinear wave modulation between a high frequency probing wave and a low frequency pumping wave. Finally, other types of nonlinearity may be considered in the FE model, thus extending the possible applications of the method.

References

- [1] I.Y. Solodov, N. Krohn, G. Busse, CAN: an example of nonclassical acoustic nonlinearity in solids, Ultrasonics 40 (2002) 621-625.
- [2] K. Van Den Abeele, P.A. Johnson, A. Sutin, Nonlinear Elastic Wave Spectroscopy (NEWS) techniques to Discern Material Damage, Part I: Nonlinear Wave Modulation Spectroscopy (NWMS), J. Nondestruct. Eval. 12 (2000) 17–30.
- [3] D. Donskoy, A. Sutin, A. Ekimov, Nonlinear acoustic interaction on contact surfaces and its use for nondestructive testing, NDT & E Int. 34 (2001) 231–238.
- [4] Y. Zheng, R.G. Maev, I.Y. Solodov, Nonlinear acoustic applications for material characterization: a review, Can. J. Phys. 77 (1999) 927–967.
- [5] K.-Y. Jhang, Nonlinear ultrasonic techniques for nondestructive assessment of micro damage in material: A review, Int. J. Precis. Eng. Manuf. 10 (1) (2009) 123–135.
- [6] C. Pecorari, Nonlinear interaction of plane ultrasonic waves with an interface between rough surfaces in contact, J. Acoust. Soc. Am. 113 (6) (2003) 3065–3072.
- [7] C. Pecorari, M. Poznic, Nonlinear acoustic scattering by a partially closed surface-breaking crack, J. Acoust. Soc. Am. 117 (2) (2005) 592–600.
- [8] S. Biwa, S. Hiraiwa, E. Matsumoto, Pressure-dependent stiffnesses and nonlinear ultrasonic response of contacting surfaces, J. Solid Mech. Mater. Eng. 3 (1) (2009) 10–21.
- [9] J.-Y. Kim, A. Baltazar, J.W. Hu, S.I. Rokhlin, Hysteretic linear and nonlinear acoustic responses from pressed interfaces, Int. J. Solids Struct. 43 (2006) 6436–6452
- 6436–6452. [10] R.A. Guyer, K.R. McCall, G.N. Boitnott, Hysteresis, discrete memory, and nonlinear wave propagation in rock: A new paradigm, Phys. Rev. Lett. 74 (1995) 3491–3494.
- [11] M. Scalerandi, V. Agostini, P.P. Delsanto, K.E.-A. Van Den Abeele, P.A. Johnson, Local interaction simulation approach to modeling nonclassical, nonlinear behavoir in solids, J. Acoust. Soc. Am. 113 (2003).
- [12] F. Ciampa, E. Barbieri, M. Meo, Modelling of multiscale nonlinear interaction of elastic waves with three-dimensional cracks, J. Acoust. Soc. Am. 135 (6) (2014) 3209–3220. http://www.ncbi.nlm.nih.gov/pubmed/24907786.
- [13] D.A. Mendelsohn, J.M. Doong, Transient dynamic elastic frictional contact: a general 2D boundary element formulation with examples of SH motion, Wave Motion 11 (1989) 1–21.
- [14] S. Hirose, J.D. Achenbach, Higher harmonics in the far field due to dynamic crack-face contacting, J. Acoust. Soc. Am. 93 (1) (1993) 142–147.
- [15] S. Hirose, 2-D scattering by a crack with contact-boundary conditions, Wave Motion 19 (1993) 37–49.
- [16] P. Blanloeuil, A. Meziane, C. Bacon, Numerical study of nonlinear interaction between a crack and elastic waves under an oblique incidence, Wave Motion 51 (3) (2014) 425–437.
- [17] J.T. Hunt, M.R. Knittel, D. Barach, Finite element approach to acoustic radiation from elastic structures, J. Acoust. Soc. Am. 55 (2) (1974) 269–280.
- [18] J.T. Hunt, M.R. Knittel, C.S. Nichols, D. Barach, Finite-element approach to acoustic scattering from elastic structures, J. Acoust. Soc. Am. 57 (2) (1975) 287–299.
- [19] A.J. Croxford, P.D. Wilcox, B.W. Drinkwater, P.B. Nagy, The use of non-collinear mixing for nonlinear ultrasonic detection of plasticity and fatigue, J. Acoust. Soc. Am. 126 (5) (2009) 117–122.
- [20] A. Demcenko, R. Akkerman, P.B. Nagy, R. Loendersloot, Non-collinear wave mixing for non-linear ultrasonic detection of physical ageing in PVC, NDT & E Int. 49 (0) (2012) 34–39.
- [21] E. Escobar-Ruiz, A. Ruiz, W. Hassan, D.C. Wright, I.J. Collison, P. Cawley, P.B. Nagy, Non-linear ultrasonic NDE of titanium diffusion bonds, J. Nondestruct. Eval. (2013) 1–9.
- [22] P. Blanloeuil, A. Meziane, C. Bacon, 2D finite element modeling of the non-collinear mixing method for detection and characterization of closed cracks, NDT & E Int. 76 (2015) 43–51. http://www.sciencedirect.com/science/article/pii/S0963869515000833, http://linkinghub.elsevier.com/retrieve/pii/S0963869515000833.
- [23] L. Baillet, T. Sassi, Mixed finite element methods for the Signorini problem with friction, Numer. Methods Partial Differential Equations 22 (6) (2006) 1489–1508
- [24] P.G. Ciarlet, The Finite Element Method for Elliptic Problems, Elsevier, 1978.
- [25] M. Jean, The non-smooth contact dynamics method, Comput. Methods Appl. Mech. Engrg. 177 (3-4) (1999) 235-257.
- [26] N.J. Carpenter, R.L. Taylor, M.G. Katona, Lagrange constraints for transient finite element surface contact, Internat. J. Numer. Methods Engrg. 32 (1) (1991) 103–128.
- [27] L. Baillet, T. Sassi, Mixed finite element formulation in large deformation frictional contact problem, Rev. Européenne Élém. Finis 14 (2–3) (2005) 287–304.
- [28] B. O'Neill, R. Maev, F. Severin, Distortion of shear waves passing through a friction coupled interface, in: Review of Progress in Quantitative Nondestructive Evaluation, Vol. 557, AIP, 2001, pp. 1264–1267.
- [29] P. Blanloeuil, A.J. Croxford, A. Meziane, Numerical and experimental study of the nonlinear interaction between a shear wave and a frictional interface, J. Acoust. Soc. Am. 135 (4) (2014) 1709–1716. http://scitation.aip.org/content/asa/journal/jasa/135/4/10.1121/1.4868402.
- [30] S. Liu, A.J. Croxford, S.A. Neild, Z. Zhou, Effects of experimental variables on the nonlinear harmonic generation technique, IEEE Trans. Ultrason. Ferroelectr. Freq. Control 58 (2011) 1142–1451.
- [31] H. Okada, K. Harumi, S. Watanabe, Reflection of elastic waves by an infinitely long ribbon crack (part II), Japan. J. Appl. Phys. 21 (S3) (1982) 120–122.
- [32] G.L. Jones, D.R. Kobett, Interaction of elastic waves in an isotropic solid, J. Acoust. Soc. Am. 35 (1) (1963) 5–10.
- [33] F.R. Rollins, Interaction of ultrasonic waves in solid media, Appl. Phys. Lett. 2 (8) (1963) 147-148.
- [34] Z. Zhang, P.B. Nagy, W. Hassan, Analytical and numerical modeling of non-collinear shear wave mixing at an imperfect interface, Ultrasonics 65 (2016) 165–176.